*Journal of Ceramic Processing Research. Vol. 21, Special. 1, pp. s33~s40 (2020)*
*(Received 19 December 2019, Received in revised form 31 March 2020, Accepted 14 April 2020)*
*https://doi.org/10.36410/jcpr.2020.21.S1.s33*

J O U R N A L O F
**Ceramic Processing Research**

# $Cu_3Se_2$ counter electrode with rGO interlayer by pulsed electrodeposition for quantum dot-sensitized solar cells

**Yong-Han Yun, In-Rok Jo, Young-Hoon Lee, Vu Hong Vinh Quy and Kwang-Soon Ahn***
*School of Chemical Engineering, Yeungnam University, Gyeongsan 712-749, Republic of Korea*

**We synthesized a reduced graphene oxide/copper selenide (rGO/$Cu_3Se_2$) cumulative structure on a fluorine doped tin oxide (FTO) conducting glass substrate. The pulsed electrodeposition method was used to construct the rGO and $Cu_3Se_2$ nanostructures. During rGO deposition, pulsed electrodeposition resulted in a uniform film on the FTO. Deposited rGO with surface defects can act as an active site for $Cu_3Se_2$ growth. In the case of $Cu_3Se_2$, pulsed electrodeposition contributed to its uniform stoichiometry and porous structure. This porosity affected the efficient diffusion of liquid electrolytes toward the counter electrode surface and resulted in high power conversion efficiency. In addition, the rGO interfacial layer served as electron shuttle, directly prohibited the recombination path between the FTO and electrolyte and enhanced the fill factor (FF). As a result, the FTO/rGO/$Cu_3Se_2$ electrodes with CdS/CdSe/ZnSe QD photoanodes achieved a power conversion efficiency of 3.622%, which was a significant improvement over the 2.997% efficiency of direct-deposited FTO/$Cu_3Se_2$ electrodes with the same photoanodes.**

**Keywords: Quantum dot-sensitized solar cells, Reduced graphene oxide, Copper selenide, Pulsed electrodeposition, Counter electrode.**

## Introduction

Quantum Dot-sensitized Solar Cells (QDSSCs) are third generation solar cells that have the potential to overcome the Shockely-Queisser limit in the power conversion efficiency (PCE) of Si-based solar cells [1]. They have a similar structure to dye-sensitized solar cells, but the dyes are replaced with inorganic quantum dots (QDs). A QD photosensitizer has more advantageous and unique properties than organic dyes, including a size dependent band gap, hot carrier injection, and multiple exciton generation. [2-4]. Most studies on QDSSCs have focused on enhancing the performance of photoanodes to improve its light absorbing efficiency and electron injection and preventing recombination [5-7]. However, despite their importance, there remains an insufficient number of studies on counter electrode materials. As part of the QDSSC, the counter electrode plays an important role in the reduction of electrolytes and maintenance of the polysulfide electrolyte condition [3]. Even though the photoanode displays sufficient performance, completion of QDSSC operations requires a stable and efficient counter electrode [8, 9]. However, stable counter electrodes with polysulfide are a contentious issue [10-12]. Most of the known materials used for counter electrodes exhibit only limited stability against polysulfide electrolytes [4]. It is for this reason that many researchers continue to investigate stable counter electrode materials. Among them, metal chalcogenides are a promising material for counter electrodes owing to their good bulk conductivity and electrocatalytic properties [13]. To enhance stability, some researchers have suggested that a combination with a carbon based material is effective. [9] Reduced graphene oxide (rGO), in particular, has arisen as the most prominent candidate [14, 15]. The rGO has been investigated by many researchers owing to its higher conductivity than graphene oxide and surface area. Furthermore, it is proved that rGO interfacial layer has benefit when adopted at photoanode and counter electrode both [16-18]. Wang et al adopted rGO layer between FTO and $TiO_2$ film as interfacial layer to prevent direct contact with electrolyte from CdS QD [16]. This rGO layer also supports transportation of electron, can be exploited in opposite side. In case of counter electrode application, Jie Ma et al exploited graphene aerogel for using its extreme surface area to support $MoS_2$ [17]. Wei Lu's group has studied direct synthesis of copper sulfides on rGO sheets. During hydrothermal synthesis, $Cu_2S$ is embedded in rGO as nano particle and GO is reduced into rGO. They spin coated rGO-CuS paste with ethanol and PEG on FTO for counter electrode, achieved 4.76% in PCE [19]. However, binder may limit efficient diffusion of electrolyte along the porous structure. Binder-assisted adhesion also may cause instable conduction and degradation. However electrochemical process can grow rGO and active materials onto substrate directly. Under precise control of deposition condition, electrochemically grown crystals exhibits robust contact with substrate.

*Corresponding author:
Tel : +82-53-810-2524
Fax: +82-53-810-4631
E-mail: kstheory@ynu.ac.kr

Additionally, it is well known that electro pulse-deposition (EPD) can induce unique results [20] and give a uniform composition to the resulting product, such as a thin film on the substrate [21]. To the best of our knowledge, there are only a few studies that have applied both pulse-deposited copper selenide ($Cu_3Se_2$) and rGO in order to fabricate counter electrodes for QDSSCs. Zeng et al. (2016) made a thin lead selenide film on FTO using pulsed voltage deposition [22]. Ahn et al. (2019) used a similar approach for nickel selenides [23]. In this study, we introduce pulsed electro-deposited rGO and $Cu_3Se_2$ electrodes for the counter electrodes of QDSSCs.

## Experimental Section

### GO preparation

Synthesis of graphene oxide (GO) was followed by the Hummer's method from literature [24]. One gram of graphite powder was mixed with 23 ml of $H_2SO_4$ (concentrated, 95%) under ice bath and mild stirring conditions. One gram of $NaNO_3$ was dissolved in the mixture after adequate dissolution. Three grams of $KMnO_4$ was slowly added in portion. The temperature was kept under 20 ? during the addition of the $KMnO_4$. The color of mixture turned from a graphite grey/black to a dark green. After two hours of stirring under ice bath conditions, 46 ml of deionized (D.I.) water was introduced into the mixture. Simultaneously, the temperature of the mixture was kept under 98 ?. At that point, vigorous stirring was performed for two hours. To complete the reaction and eliminate excessive elements in the mixture, 140 ml of D.I. water and 2 ml of $H_2O_2$ (30%) were added. The color immediately changed to a bright yellow. After 15 min of stirring, 250 ml of diluted 1 M HCl aqueous solution was added to the mixture to dissolve any metallic by-products. After washing with DI water three times and centrifugation, brown precipitates were formed. By dissolving and dispersing the proper amount of this product in D.I. water, 1 mg/ml of a GO solution was synthesized for further use.

### GO and Cu-EDTA solution for electrodeposition of an rGO layer

An ethylenediaminetetraacetic acid (EDTA) capped copper (Cu-EDTA) solution was made by following literature [22, 25]. Simply, 0.5954 g of EDTA was dissolved in 20 ml of D.I. water. This was followed with 0.128 g of NaOH to adjust the pH beyond 12. Then, 0.1996 g of $CuSO_4$ was added. One milliliter of the Cu-EDTA solution was mixed with 39 ml of GO solution. The prepared solution was stable after being kept in the dark under ambient air conditions for a few days. Using the prepared solution, an rGO layer was electrodeposited onto FTO. Detailed conditions of the electrodeposition are described in Table 1.

**Table 1.** Overview of pulsed electrodeposition parameters for preparation of rGO and copper selenide.

| Parameters | rGO | Copper selenide |
|---|---|---|
| Forward | -5 (mA/cm$^2$) | -0.1 (V) |
| Reverse | 0 (mA/cm$^2$) | 0.4 (V) |
| $T_{on}$ [sec] | 0.1 | 0.5 |
| $T_{off}$ [sec] | 0.1 | 1.0 |
| Total T [sec] | 180 | 1260 |
| Effective T [sec] | 90 | 840 |

### Cu and Se precursor solution for electrodeposition of a $Cu_3Se_2$ layer

To begin, 4.9937 g of $CuSO_4$ and 2.2192 g $SeO_2$ were used to prepare 0.2 M of a Cu and Se precursor solution. The pH value of both solutions was adjusted to a value of 2 using $H_2SO_4$. Twenty milliliters of each solution were mixed together to produce a final volume of 40 ml. A solution containing the precursors was prepared and mixed just before deposition. Milli-Q pure water was used as the solvent for each solution. This prepared solution was used to deposit $Cu_3Se_2$ onto FTO and rGO modified FTO. Detailed conditions of the electrodeposition are described in Table 1.

### Photoanode for QDSSC sensitized with QDs

Preparation of the photoanodes followed the conventional successive ion layer adsorption and reaction (SILAR) method with slight modifications [6, 26]. First, the FTO was prepared using a typical cleaning method that utilizes successive ultra-sonication through acetone, ethanol, and D.I. water, respectively. A $TiO_2$ film was prepared by the doctor-blading method with a $TiO_2$ paste (Ti-Nanoxide T/SP, 20 nm diameter, Solaronix SA) on the FTO substrate. $TiO_2$ films on the FTO were dried at 70 ? over 30 min and sintered at 450 ? for 30 min under ambient air conditions. After sintering, the CdS and CdSe QDs were decorated onto the $TiO_2$ film by the SILAR method. The preparation of Cd and S precursor solutions followed literature [6]. To begin, 0.1 M of $Cd(NO_3)_2$ was dissolved in ethanol and 0.1 M of $Na_2S$ was dissolved in methanol. Each dipping process took one minute, and five cycles were done for CdS. A similar procedure was performed for CdSe. The preparation of Cd and Se precursor solutions also followed the literature referenced above. First, 0.03 M $Cd(NO_3)_2$ was dissolved in ethanol, while 0.03 M $SeO_2$ and 0.06 M $NaBH_4$ were dissolved in ethanol. Selenium dioxide solution caused the color to change from an opaque red to transparent after stirring under sealed conditions. Each dipping took one minute, and seven cycles were done for CdSe. The deposition of CdSe was conducted under inert Ar gas conditions. Next, ZnSe was deposited by the SILAR method, where it acted as a passivation layer for CdS/CdSe QDs [6, 7]. Then, 0.1 M $Zn(NO_3)_2$, 0.1 M $SeO_2$, and 0.2 M $NaBH_4$ were dissolved in ethanol. Each cycle took one minute,

and five cycles were done for ZnSe. After the SILAR process, every photoanode was washed with ethanol and kept in the dark under inert gas conditions for further use.

### Material characterization

The surface morphology and cross section of each sample was observed by high-resolution scanning electron microscopy (HR-SEM; S-4800, Hitachi LTD). The structure and crystallinity were characterized through X-ray diffraction (XRD; MPD for thin film, DIATOME). To investigate the surface atomic state and confirm the atomic ratio, X-ray photo-electron spectroscopy (XPS; K-alpha, Thermo Fisher Scientific) was conducted.

### Device performance characterization

Symmetrical dummy cells for the Tafel analysis and electrochemical impedance spectra (EIS) were prepared by two identical counter electrodes. The polysulfide electrolytes used in the symmetrical cells had the same composition (2 M Sulfur, 2 M $Na_2S$, and 0.2 M KCl) as the full cell with a solvent composed of methanol and water (7:3 by volume) [12,37,38]. The active area of the symmetrical cell was 1.2 $cm^2$ for every sample and experiment. The Tafel polarization (WBCS3000, WONATECH) was recorded from -0.5 V to 0.5 V at a scan rate of 10 mV/s. An EIS (ZIVE, WONATECH) analysis was carried out to understand the electrochemical reaction around the surface of the electrodes. The PCE was measured under 1-sun illumination by solar simulator (PEC-L12 Solar Simulator, Peccell technology, Inc.) and potentiostat (Iviumstat.h, Ivium technologies).

## Results and Discussion

### Structure and morphology

Reduced graphene oxide (rGO) and umangite copper selenide ($Cu_3Se_2$) layers were successively deposited onto an FTO substrate. The rGO-modified FTO had many surface defects [29] that provided active sites for copper selenide growth. These sites may also provide different orientations compared with direct deposition onto FTO. The effect of rGO-modified FTO was confirmed via XRD. According to Fig. 1, the $Cu_3Se_2$ on FTO displayed a typical peak known as umangite (JCPDS 00-047-1745). The $Cu_3Se_2$ on rGO-modified FTO displayed a similar peak, but a difference in the peak intensity was observed. This difference came from the presence of different orientations due to the active sites provided by the rGO-modified FTO. The $Cu_3Se_2$ on FTO, (101) displayed the dominant peak along the FTO. It should be noted that the deposited selenium induced the reduction of copper ions to form copper selenide [30, 31]. However, on the rGO-modified FTO, copper was already deposited on the surface of the rGO [20, 25]. The Cu-EDTA-GO solution was used to deposit the rGO and facilitated the

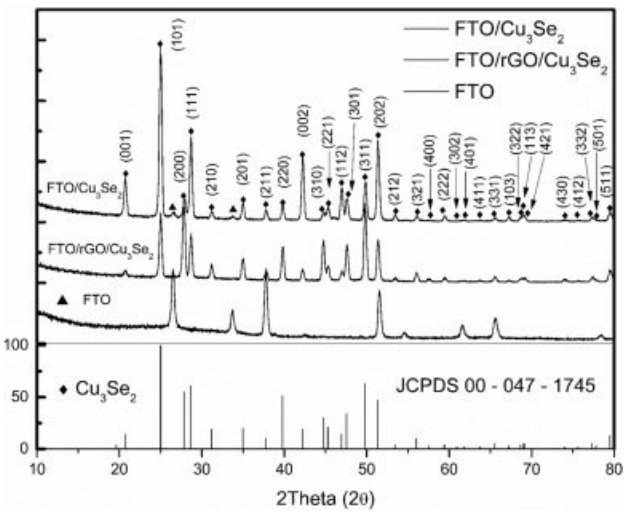


**Fig. 1.** XRD results of FTO/$Cu_3Se_2$, FTO/rGO/$Cu_3Se_2$ and FTO.

presence of copper on the rGO as a metallic cluster. According to the electrodeposition mechanism of copper selenide, selenium is first deposited on the substrate followed by the reduction of the copper ions [30].

When selenium was deposited onto Cu, the presence of the copper contributed to different preferential orientations of the copper selenide. This is likely the reason for the reversed intensity between the $Cu_3Se_2$ (200) and (111) at the $Cu_3Se_2$ on the rGO modified sample. To understand the effect of surface modifications on the morphology, SEM was conducted on each sample. Fig. 2 shows the top view and cross-section of each sample. Fig. 2(a) shows a conventional Pt electrode to compare with the other samples. Fig. 2(b) shows an rGO-modified FTO. It is clear that the rGO uniformly covered the FTO, and the copper clusters were regularly distributed as well. From Fig. 2(c) and 2(d), the significant effects of different substrates on the morphology can be seen. Fig. 2(c) shows a morphology that is vastly different from typical copper selenide because of the pulsed electrodeposition technique [21]. During pulsed electrodeposition in the forward condition, copper selenide was deposited onto FTO. During the reverse condition, the precursor concentration at the interface was restored to near the initial condition by mass transfer and diffusion. By iterating this cycle, tiny pillars that aggregated into square–like columns were grown. In Fig. 2(d), the Cu on the rGO provided more active sites than the FTO, which led to a more porous film. This enhanced porosity may help to diversify the paths available for the active mass transfer of electrolytes. However, observations from Fig. 2(f) and (g) may indicate that the growth mechanisms of each film are similar to that of other work [21]. The height of the films on the different substrates were not significantly different from each other. The microstructure of the rGO/$Cu_3Se_2$ sample was further investigated by transmission electron microscopy (TEM). Fig. 3(a-c) show the

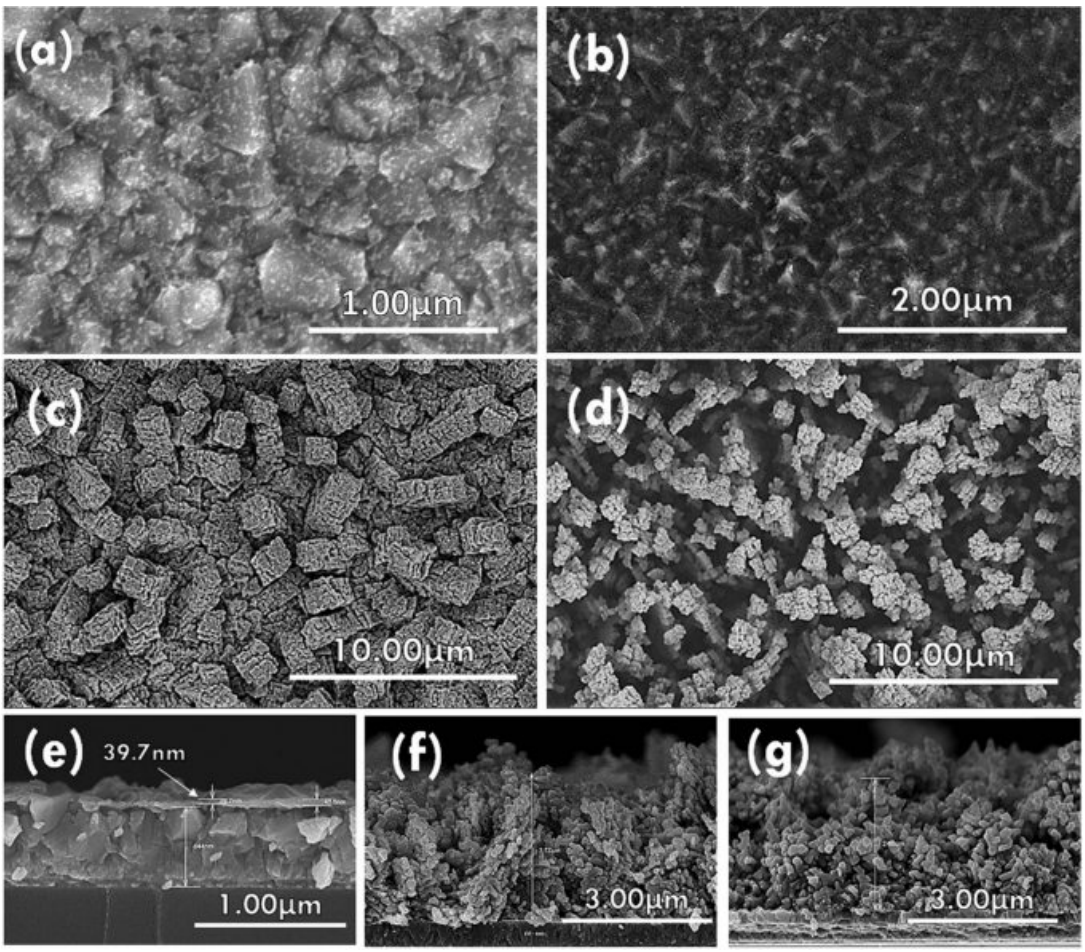


**Fig. 2.** SEM images of electrode surface, (a) FTO/Pt, (b) FTO/rGO, (c) FTO/$Cu_3Se_2$ (d) FTO/rGO/$Cu_3Se_2$ and (e-g) are cross section of (b-d) respectively.

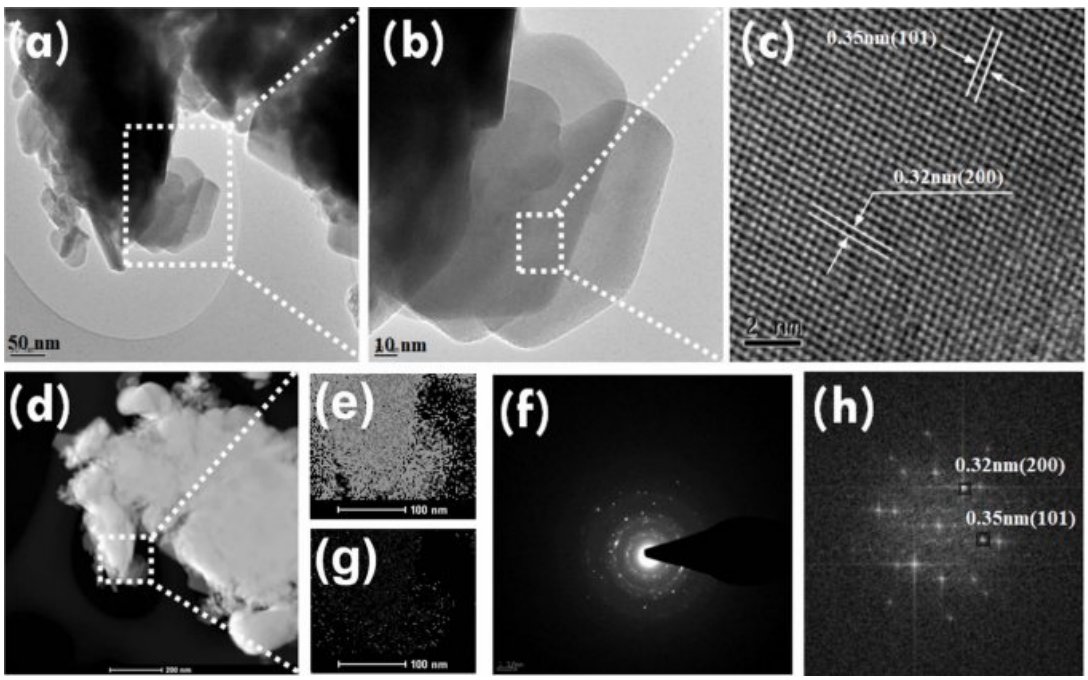


**Fig. 3.** (a-c) TEM and HRTEM images of $Cu_3Se_2$, (d) EDAX objective area, (e, f) Cu and Se elemental mapping in scan area, (g) SAED pattern of sample and (h) FFT from (c).

crystalline nature of $Cu_3Se_2$ on rGO. The results from Fig. 3(c) confirmed (101) and (200) planes of umangite (JCPDS 00-047-1745), which corresponded well to the results obtained via XRD. The loading densities of $Cu_3Se_2$ deposited on FTO and FTO/rGO were 0.3106 g/cm$^3$ and 0.2938 g/cm$^3$, respectively.

While $Cu_3Se_2$ has been well characterized, there is still a lack of significant understanding of rGO. To confirm the degree of reduction and existence of rGO on FTO, Raman spectroscopy was used to measure each electrode. In Fig. 4(a), conventional D and G peaks can be observed. This indicated that GO was successfully synthesized and well oxidized [32, 33].

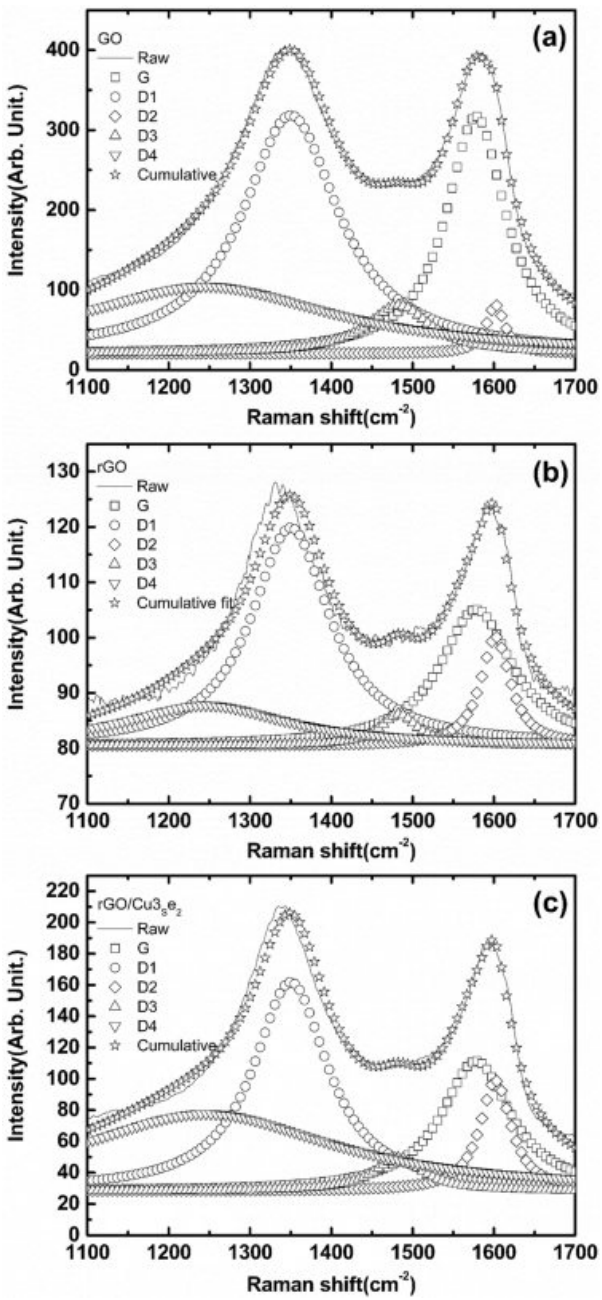


**Fig. 4.** Raman spectra of (a) GO, (b) rGO, (c) rGO/$Cu_3Se_2$.

The deconvolution of Fig. 4(a) also corresponded to the above prediction. Fig. 4(b) shows a diminished G peak, which indicated a reduction of the oxygen containing group [39]. Fig. 4(c) shows similar results. To verify the degree of reduction and other information, the D/G ratio was calculated from the deconvoluted peaks [29, 33, 34]. Table 2 shows the D/G ratios determined from the Raman spectroscopy of GO, rGO, and rGO/$Cu_3Se_2$ deposited FTO. The D/G ratio is an important index designating characteristic for graphene and graphene-like materials. A larger D/G ratio indicates that a smaller graphene oxide flake size was achieved [33]. It also indicates the presence of more edge defect sites. An abundant number of defects can serve as active sites for $Cu_3Se_2$ growth as mentioned previously. A high D/G ratio can also indicate the removal of oxygen-containing groups [35-37].

To support the above characterization, XPS was done on the rGO/$Cu_3Se_2$ sample [38]. Fig. 5 shows the XPS spectra of (a) C 1s, (b) O 1s, (c) Cu 2p, and (d) Se 3d from the rGO/$Cu_3Se_2$ sample. Fig. 5(a) suggests that the rGO was well reduced by the pulsed electrodeposition process. C-C strongly remained at 284 eV. The peak value at 284 eV indicated C-C bonds relevant with sp2 and sp3. There were slightly low residues for the C-O, C=O, O=C-O peaks. This indicated that the reduction of GO was successful during electrodeposition. It also corresponded well to the results obtained via Raman spectroscopy. The broad peak around 283 eV was related to the metallic C [39], and as Cu was adsorbed onto the rGO, that peak proved the existence of copper clusters. The relatively small peaks at 286.5 eV, 287.8 eV, and 289.1 eV corresponded to the results from the D/G ratio Raman spectroscopy, and indicated the extinction of oxygen containing groups [38]. From the deconvoluted XPS peak areas, the C/O ratio was calculated to be 8.944. This indicated an adequate reduction of rGO on the FTO. This result corresponded to the results from the Raman spectroscopy.

## Morphology-dependent device performance

The electrochemical activity of the prepared CEs was analyzed by Tafel analysis EIS. Fig 6(a) shows the Tafel polarization curves of the Pt, $Cu_3Se_2$ and rGO/$Cu_3Se_2$ CEs. Among these CEs, rGO/$Cu_3Se_2$ exhibited the highest limiting current density ($J_{lim}$). The porous structure of the $Cu_3Se_2$ grown on rGO provided more electrocatalytic active sites, which lead the superior mass transfer. Fig. 6(b-d) show the Nyquist plots of different symmetrical cells and the fitting parameters are listed in Table 3, where $R_S$ the series resistance and $R_{ct}$ is the charge transfer resistance between the CE and

**Table 2.** Peak ratios from Raman spectra.

| | GO | rGO | rGO/$Cu_3Se_2$ |
|---|---|---|---|
| $I_D$ / $I_G$ | 1.018 | 1.599 | 1.608 |

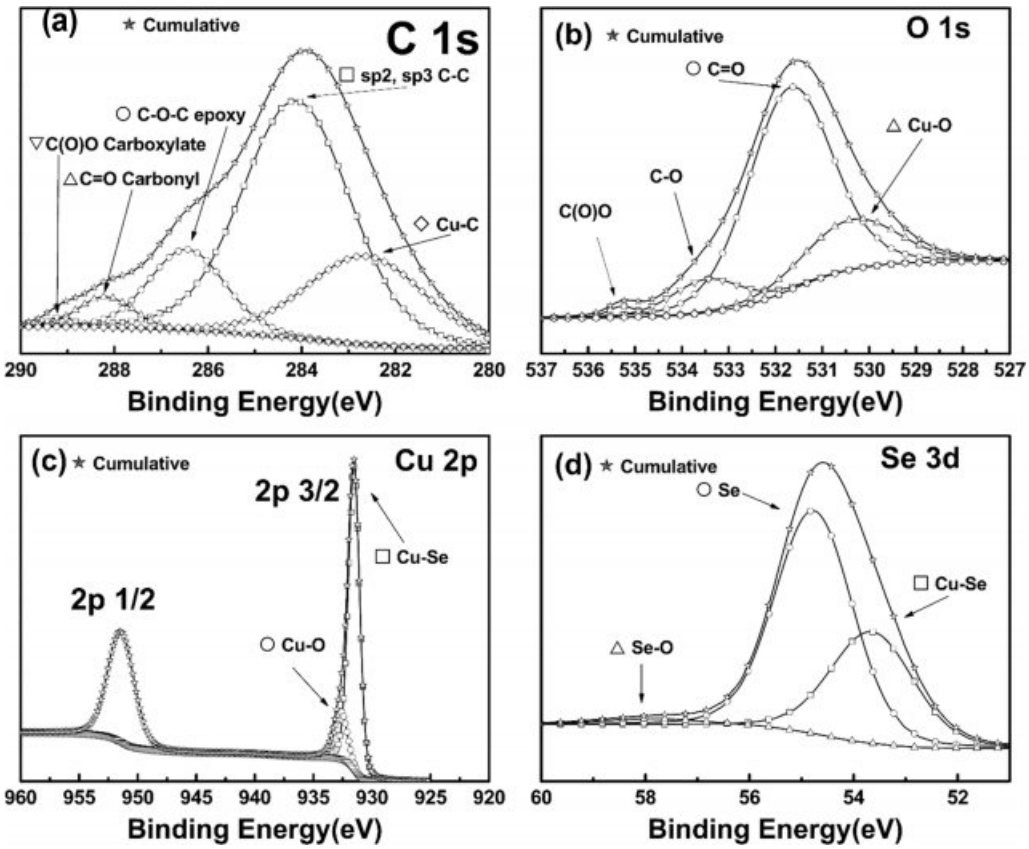


**Fig. 5.** XPS spectra of (a) C 1s, (b) O 1s, (c) Cu 2p and (d) Se 3d from FTO/ rGO/$Cu_3Se_2$.

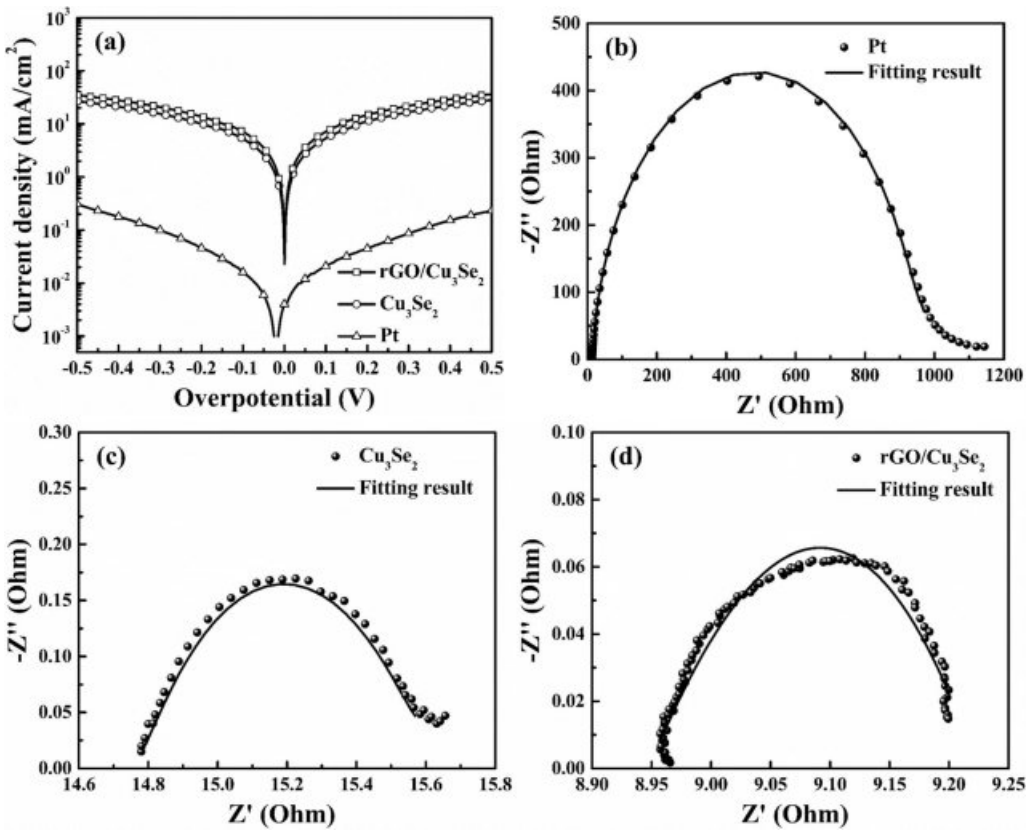


**Fig. 6.** (a) Tafel polarization curves from symmetrical cells of Pt, $Cu_3Se_2$ and rGO/$Cu_3Se_2$**.** Nyquist plots of (b) Pt, (c) $Cu_3Se_2$ and (d) rGO/ $Cu_3Se_2$.

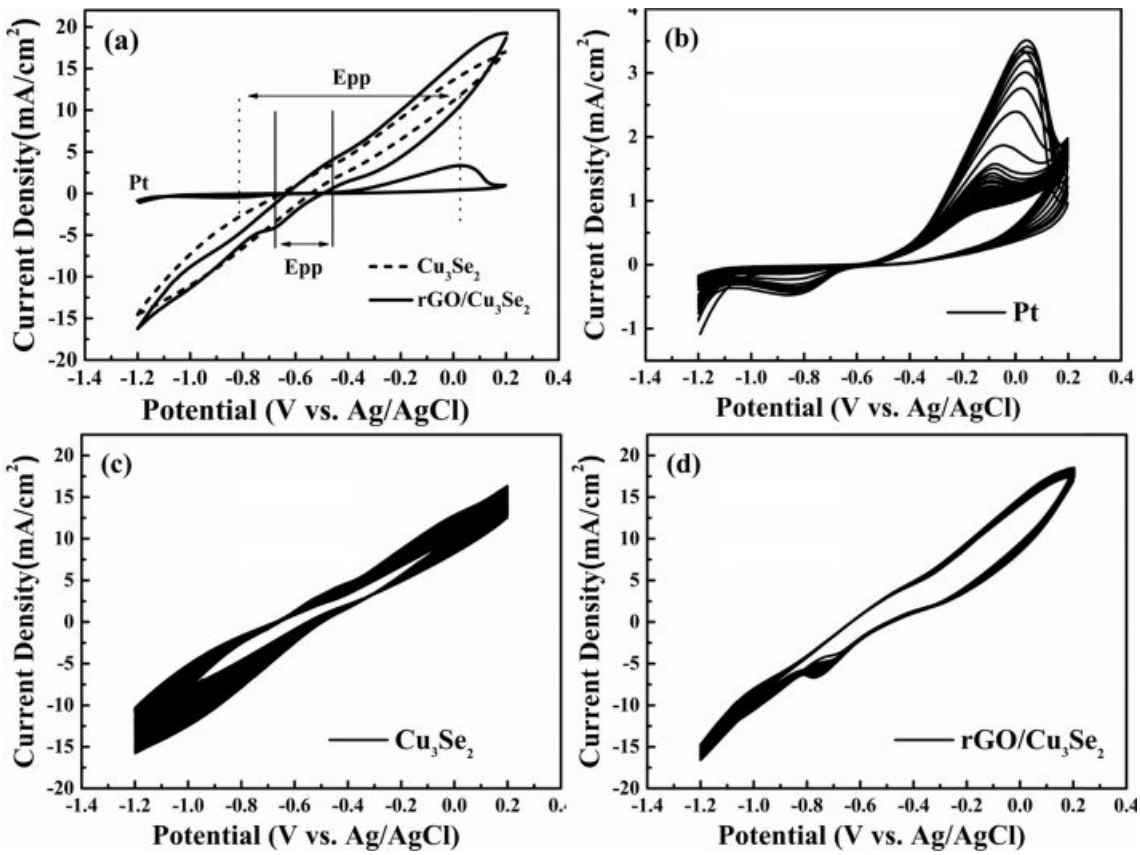


**Fig. 7.** (a) Cyclic voltammetry curves of CEs. Cycling stability tests for 50 cycles of (a) Pt, (b) $Cu_3Se_2$ and (c) rGO/$Cu_3Se_2$.

electrolyte. The $R_{ct}$ values of Pt, $Cu_3Se_2$ and rGO/$Cu_3Se_2$ CEs were 844.9, 1.15 and 0.292 Ω, respectively. This result shows the rGO/$Cu_3Se_2$ CE has superior charge transfer kinetics which can affect in FF.

Cyclic voltammetry (CV) was performed to evaluate the electrocatalytic activity and electrochemical stability. The oxidation and reduction peak current and peak-to-peak potential difference (Epp) are simple and powerful tool for estimate the electrocatalytic activity [40, 41]. Both $Cu_3Se_2$ and rGO/$Cu_3Se_2$ electrodes with high electrocatalytic activity showed the lower Epp value than Pt as shown in Fig. 7(a). Meanwhile the oxidation and reduction peak positions of $Cu_3Se_2$ and rGO/$Cu_3Se_2$ electrodes are very similar, the current densities of the oxidation and reduction peaks of rGO/$Cu_3Se_2$ electrode is greater than that of the unmodified $Cu_3Se_2$ electrode. It shows that the $Cu_3Se_2$, which grown on rGO, has a higher surface area due to the porous morphology as observed in SEM. Fig. 7(b-d) show the CV curves of different CEs for 50 cycles. Pt CE has very low current density owing to their poor electrocatalytic activity and stability. $Cu_3Se_2$ CE has a higher current compared to Pt but shows apparent current decay which means low stability. rGO/$Cu_3Se_2$ CE has an excellent electrochemical stability in polysulfide electrolyte. Fig. 8 and Table 4 show the J-V curves and parameters of the QDSSCs with different CEs. QDSSC with rGO/$Cu_3Se_2$ CE has the significantly improved FF of 53.59% and PCE of 3.622% compared to $Cu_3Se_2$ CE.

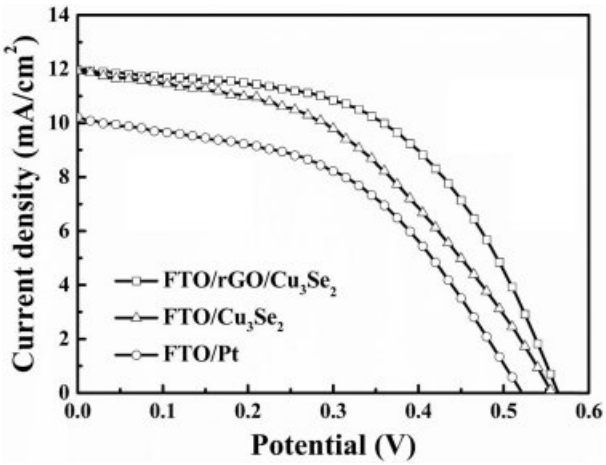


**Fig. 8.** J-V curves of Pt, $Cu_3Se_2$ and rGO/$Cu_3Se_2$ electrodes.

**Table 4.** J-V curve results.

| | Pt | $Cu_3Se_2$ | rGO/$Cu_3Se_2$ |
|---|---|---|---|
| $V_{oc}$ (V) | 0.520 | 0.555 | 0.565 |
| $J_{sc}$ (mA/cm$^2$) | 10.22 | 11.92 | 11.96 |
| FF (%) | 47.81 | 45.29 | 53.59 |
| PCE (%) | 2.540 | 2.997 | 3.622 |

## Conclusion

An rGO/$Cu_3Se_2$ layered structure was successfully synthesized onto an FTO substrate through the facile electrodeposition process. A GO solution composed of Cu-EDTA provided a uniform rGO film on the FTO substrate. The rGO layer provided active sites for $Cu_3Se_2$ growth and also prevented direct contact of the electrolyte with the FTO substrate, which suppressed recombination. Pulsed electrodeposition resulted in the stoichiometric formation of $Cu_3Se_2$ on rGO-modified FTO. The deposition of $Cu_3Se_2$ on rGO modified FTO achieved stability under ambient air conditions and a much more porous structure than the direct formation of $Cu_3Se_2$ on FTO. A strong dependence between the morphology and mass transfer of electrolytes was observed. The porous structure induced the rGO layer to $Cu_3Se_2$ and led to the enhanced performance of the QDSSC from the increased FF and $J_{lim}$.

## Acknowledgements

This work was supported by the 2019 Yeungnam University Research Grant. This study was also supported by the "Human Resources Program in Energy Technology" of the Korea Institute of Energy Technology Evaluation and Planning (KETEP), supported by the Ministry of Trade, Industry & Energy, Republic of Korea (No. 20174030201760).

## References

1. M.C. Beard, J.M. Luther, O.E. Semonin and A.J. Nozik, Acc. Chem. Res. 46[6] (2013) 1252-1260.
2. D.M. Chapin, C.S. Fuller and G.L. Pearson, J. Appl. Phys. 25[5] (1954) 676-677.
3. S. Kumar, M. Nehra, A. Deep, D. Kedia, N. Dilbaghi and K.-H. Kim, Renew. Sustain. Energy Rev. 73 (2017) 821-839.
4. P.V. Kamat, J. Phys. Chem. C. 112[48] (2008) 18737-18753.
5. F. Huang, J. Hou, H. Wang, H. Tang, Z. Liu, L. Zhang, Q. Zhang, S. Peng, J. Liu, and G. Cao, Nano Energy. 32 (2017) 433-440.
6. J. Tian, R. Gao, Q. Zhang, S. Zhang, Y. Li, J. Lan, X. Qu, and G. Cao, J. Phys. Chem. C. 116[35] (2012) 18655-18662.
7. F. Huang, J. Hou, Q. Zhang, Y. Wang, R. Massé, S. Peng, H. Wang, J. Liu, and G. Cao, Nano Energy. 26 (2016) 114-122.
8. I. Rauf and P. Rezai, Renew. Sustain. Energy Rev. 73 (2017) 408-422.
9. P.N. Kumar, A. Kolay, S.K. Kumar, P. Patra, A. Aphale, A.K. Srivastava and M. Deepa, ACS Appl. Mater. Interfaces. 8[41] (2016) 27688-27700.
10. B. Zhang, H. Yuan, X. Zhang, D. Huang, S. Li, M. Wang and Y. Shen, ACS Appl. Mater. Interfaces. 6[23] (2014) 20913-20918.
11. Y.-L Lee and C.-H. Chang, J. Power Sources. 185[1] (2008) 584-588.
12. H.K. Jun, M.A. Careem and A.K Arof, Int. J. Photoenergy. 2013 (2013) 1-10.
13. H.M. Choi, I.A. Ji and J.H. Bang, ACS Appl. Mater. Interfaces. 6[4] (2014) 2335-2343.
14. V.T. Chebrolu and H.-J. Kim, J. Mater. Chem. C. 7[17] (2019) 4911-4933.
15. Y. Zhu, S. Murali, W. Cai, X. Li, J.W. Suk, J.R. Potts and R.S. Ruoff, Adv. Mater. 22[35] (2010) 3906-3924.
16. L. Wang, J. Feng, Y. Tong and J. Liang, Int. J. Hydrog. Energy. 44[1] (2019) 128-135.
17. J. Ma, W. Shen and F. Yu, J. Power Sources. 351 (2017) 58-66.
18. S. Li, H. Min, F. Xu, L. Tong, J. Chen, C. Zhu and L. Sun, RSC Adv. 6[41] (2016) 34546-34552.
19. B. Yuan, Q. Gao, X. Zhang, L. Duan, L. Chen, Z. Mao, X. Li and W. Lü, Electrochim. Acta. 277 (2018) 50-58.
20. C.L.P. Pavithra, B.V. Sarada, K.V. Rajulapati, T.N. Rao and G. Sundararajan, Sci. Rep. 4[1] (2015) 4049.
21. A. Moysiadou, R. Koutsikou and M. Bouroushian, Mater. Lett. 139 (2015) 112-115.
22. B.B. Jin, Y.F. Wang, X.Q. Wang, and J.H. Zeng, Appl. Surf. Sci. 369 (2016) 436-442.
23. Y.-H. Lee, Y.-H. Yun, VHV. Quy, S.-H. Kang, H.S. Kim, E. Vijayakumar and K.-S. Ahn, Electrochim. Acta. 296 (2019) 364-371.
24. N.I. Kovtyukhova, P.J. Ollivier, B.R. Martin, T.E. Mallouk, S.A. Chizhik, E.V. Buzaneva, and A.D. Gorchinskiy, Chem. Mater. 11[3] (1999) 771-778.
25. Y. Mai, M. Zhou, H. Ling, F. Chen, W. Lian, and X. Jie, Surf. Sci. 433 (2018) 232-239.
26. V. Gonzalez-Pedro, X. Xu, I. Mora-Ser and J. Bisquert, ACS Nano. 4[10] (2010) 5783-5790.
27. H.J. Lee, M. Wang, P. Chen, D.R. Gamelin, S.M. Zakeeruddin, M. Grátzel, and M.K. Nazeeruddin, Nano Lett. 9[12] (2009) 4221-4227.
28. J. Yu, W. Wang, Z. Pan, J. Du, Z. Ren, W. Xuea and X. Zhong, J. Mater. Chem. A. 5[27] (2017) 14124-14133.
29. S. Pei and H.-M. Cheng, Carbon. 50[9] (2012) 3210-3228.
30. L. Li, J. Gong and W. Zhu, IOP Conf Ser Earth Environ Sci. 59[1] (2017) 012060.
31. D. Lippkow and H.H. Strehblow, Electrochim. Acta. 43[14-15] (1998) 2131-2140.
32. J. Sourice, A. Quinsac, Y. Leconte, O. Sublemontier, W. Porcher, C. Haon, A. Bordes, E.D. Vito, A. Boulineau, S.J. Larbi, N. Herlin-Boime, and C. Reynaud, ACS Appl. Mater. Interfaces. 7[12] (2015) 6637-6644.
33. A. Wang, W. Yu, Y. Fang, Y. Song, D. Jia, L. Long, M.P. Cifuentes, M.G. Humphrey and C. Zhang, Carbon. 89 (2015) 130-141.
34. S.H. Huh and S. Mikhailov, in "Physics and Applications of Graphene – Experiments" (IntechOpen, 2011) p. 73.
35. L. Zhou, X. Yang, B. Yang, X. Zuo, G. Li, A. Feng, H. Tang, H. Zhang, M. Wu, Y. Ma, S. Jin, Z. Sun and X. Chen, J. Power Sources. 272 (2014) 639-646.
36. A. Wei, L. Xiong, L. Sun, Y. Liu, W. Li, W. Lai, X. Liu, L. Wang, W. Huang and X. Dong, Mater. Res. 48[8] (2013) 2855-2860.
37. M.A. Pimenta, G. Dresselhaus, M.S. Dresselhaus, L.G. Cancado, A. Jorio and R. Saito, Phys. Chem. Chem. Phys. 9[11] (2007) 1276-1290.
38. A.G. Marrani, R. Zanoni, R. Schrebler, and E.A. Dalchiele, J. Phys. Chem. C. 121[10] (2017) 5675-5683.
39. N. Dukstiene, L. Tatariskinaite, M. Andrulevicius, Mater Sci-Poland. 28[1] (2010) 93.
40. R. Riaz, M. Ali, I.A. Sahito, A.A. Arbab, T. Maiyalagan, A.S. Anjum, M.J. Ko, S.H. Jeong, Appl. Sur. Sci. 480 (2019) 1035-1046.
41. R. Riaz, M. Ali, H. Anwer, M.J. Ko, S.H. Jeong, J. Colloid Interface Sci. 557 (2019) 174-184.